FERMILAB-PUB-18-114-CD

Prepared for submission to JINST

Calibration of the NEXT-White detector using ^{83m}Kr decays

NEXT collaboration

G. Martínez-Lema,[b,l,1] J.A. Hernando Morata,[l] B. Palmeiro,[b] A. Botas,[b] P. Ferrario,[j,t,b] F. Monrabal,[p,j] A. Laing,[b] J. Renner,[b] J.J. Gómez-Cadenas,[j,t,b,2] C. Adams,[a] V. Álvarez,[b] L. Arazi,[c] C.D.R. Azevedo,[d] K. Bailey,[n] J.M. Benlloch-Rodríguez,[b] F.I.G.M. Borges,[e] S. Cárcel,[b] J.V. Carrión,[b] S. Cebrián,[f] C.A.N. Conde,[e] J. Díaz,[b] M. Diesburg,[g] J. Escada,[e] R. Esteve,[h] R. Felkai,[b] L.M.P. Fernandes,[i] A.L. Ferreira,[d] E.D.C. Freitas,[i] J. Generowicz,[j] A. Goldschmidt,[k] D. González-Díaz,[l] R. Guenette,[a] R.M. Gutiérrez,[m] K. Hafidi,[n] J. Hauptman,[o] C.A.O. Henriques,[i] A.I. Hernandez,[m] V. Herrero,[h] S. Johnston,[n] B.J.P. Jones,[p] M.Kekic,[b] L. Labarga,[q] P. Lebrun,[g] N. López-March,[b] M. Losada,[m] J. Martín-Albo,[a] A. Martínez,[b] A.D. McDonald,[p] C.M.B. Monteiro,[i] F.J. Mora,[h] J. Muñoz Vidal,[b] M. Musti,[b] M. Nebot-Guinot,[b] P. Novella,[b] D.R. Nygren, [p,2] A. Para,[g] J. Pérez,[b] M. Querol,[b] J. Repond,[n] S. Riordan,[n] L. Ripoll,[r] J. Rodríguez,[b] L. Rogers,[p] C. Romo,[b] F.P. Santos,[e] J.M.F. dos Santos,[i] A. Simón,[b] C. Sofka,[s] M. Sorel,[b] T. Stiegler,[s] J.F. Toledo,[h] J. Torrent,[b] J.F.C.A. Veloso,[d] R. Webb,[s] J.T. White,[s,3] N. Yahlali[b]

[a]*Department of Physics, Harvard University*
Cambridge, MA 02138, USA

[b]*Instituto de Física Corpuscular (IFIC), CSIC & Universitat de València*
Calle Catedrático José Beltrán, 2, 46980 Paterna, Valencia, Spain

[c]*Nuclear Engineering Unit, Faculty of Engineering Sciences, Ben-Gurion University of the Negev*
P.O.B. 653 Beer-Sheva 8410501, Israel

[d]*Institute of Nanostructures, Nanomodelling and Nanofabrication (i3N), Universidade de Aveiro*
Campus de Santiago, 3810-193 Aveiro, Portugal

[e]*LIP, Department of Physics, University of Coimbra*
P-3004 516 Coimbra, Portugal

[f]*Laboratorio de Física Nuclear y Astropartículas, Universidad de Zaragoza*
Calle Pedro Cerbuna, 12, 50009 Zaragoza, Spain

[g]*Fermi National Accelerator Laboratory*
Batavia, Illinois 60510, USA

[1]corresponding author.
[2]NEXT Co-spokesperson.
[3]Deceased.

This document was prepared by [NEXT Collaboration] using the resources of the Fermi National Accelerator Laboratory (Fermilab), a U.S. Department of Energy, Office of Science, HEP User Facility. Fermilab is managed by Fermi Research Alliance, LLC (FRA), acting under Contract No. DE-AC02-07CH11359

[h] *Instituto de Instrumentación para Imagen Molecular (I3M), Centro Mixto CSIC - Universitat Politècnica de València*
Camino de Vera s/n, 46022 Valencia, Spain
[i] *LIBPhys, Physics Department, University of Coimbra*
Rua Larga, 3004-516 Coimbra, Portugal
[j] *Donostia International Physics Center (DIPC)*
Paseo Manuel Lardizabal 4, 20018 Donostia-San Sebastian, Spain.
[k] *Lawrence Berkeley National Laboratory (LBNL)*
1 Cyclotron Road, Berkeley, California 94720, USA
[l] *Instituto Gallego de Física de Altas Energías, Univ. de Santiago de Compostela*
Campus sur, Rúa Xosé María Suárez Núñez, s/n, 15782 Santiago de Compostela, Spain
[m] *Centro de Investigación en Ciencias Básicas y Aplicadas, Universidad Antonio Nariño*
Sede Circunvalar, Carretera 3 Este No. 47 A-15, Bogotá, Colombia
[n] *Argonne National Laboratory,*
Argonne IL 60439, USA
[o] *Department of Physics and Astronomy, Iowa State University*
12 Physics Hall, Ames, Iowa 50011-3160, USA
[p] *Department of Physics, University of Texas at Arlington*
Arlington, Texas 76019, USA
[q] *Departamento de Física Teórica, Universidad Autónoma de Madrid*
Campus de Cantoblanco, 28049 Madrid, Spain
[r] *Escola Politècnica Superior, Universitat de Girona*
Av. Montilivi, s/n, 17071 Girona, Spain
[s] *Department of Physics and Astronomy, Texas A&M University*
College Station, Texas 77843-4242, USA
[t] *IKERBASQUE*
, Basque Foundation for Science, 48013 Bilbao, Spain.

E-mail: gonzalo.martinez.lema@usc.es

ABSTRACT: The NEXT-White (NEW) detector is currently the largest radio-pure high pressure gas xenon time projection chamber with electroluminescent readout in the world. NEXT-White has been operating at Laboratorio Subterráneo de Canfranc (LSC) since October 2016. This paper describes the calibrations performed with ^{83m}Kr decays during a long run taken from March to November 2017 (Run II). Krypton calibrations are used to correct for the finite drift-electron lifetime as well as for the dependence of the measured energy on the event position which is mainly caused by variations in solid angle coverage. After producing calibration maps to correct for both effects we measure an excellent energy resolution for 41.5 keV point-like deposits of (4.55 ± 0.04) % FWHM in the full chamber and (3.88 ± 0.05) % FWHM in a restricted fiducial volume. Using naive $1/\sqrt{E}$ scaling, these values translate into FWHM resolutions of (0.592 ± 0.005) % FWHM and (0.504 ± 0.006) % at the $Q_{\beta\beta}$ energy of xenon double beta decay (2458 keV), well within range of our target value of 1%.

KEYWORDS: Neutrinoless double beta decay; TPC; high-pressure xenon chambers; Xenon; NEXT-100 experiment; Krypton; energy resolution; NEXT-White; NEW

ARXIV EPRINT: 1234.56789

Contents

1	**Introduction**	1
2	**Principle of operation and intrinsic resolution of a HPXe-EL TPC**	2
3	**Overview of the NEXT-White detector**	4
4	**Krypton calibrations**	5
5	**Data processing and event selection**	6
6	**Lifetime maps**	10
7	**Refining the energy map**	12
8	**Energy Resolution**	13
9	**Summary**	17

1 Introduction

The NEXT program is developing the technology of high-pressure xenon gas Time Projection Chambers (TPCs) with electroluminescent amplification (HPXe-EL) for neutrinoless double beta decay searches [1–5]. The first phase of the program included the construction, commissioning and operation of two prototypes, called NEXT-DEMO and NEXT-DBDM, which demonstrated the robustness of the technology, its excellent energy resolution and its unique topological signal [6–9].

The NEXT-White[1] (NEW) detector implements the second phase of the program. NEXT-White is a ∼ 1:2 scale model of NEXT-100 (the TPC has a length of 664.5 mm and a diameter of 522 mm while the NEXT-100 TPC has a length of 1300 mm and a diameter of 1050 mm), a 100 kg HPXe-EL detector, which constitutes the third phase of the program and is foreseen to start operations in 2019. NEXT-White has been running successfully since October 2016 at Laboratorio Subterráneo de Canfranc (LSC). Its purpose is to validate the HPXe-EL technology in a large-scale radiopure detector. This validation is composed of three main tasks: to assess the robustness and reliability of the technological solutions; to study in detail the background model with data, particularly the contribution to the radioactive budget of the different components, and to study the energy resolution and the background rejection power of the topological signature characteristic of a HPXe-EL. Furthermore, NEXT-White can provide a measurement of the two-neutrino double beta decay mode ($\beta\beta2\nu$).

[1]Named after Prof. James White, our late mentor and friend.

The detector started operations at LSC late in 2016. After a short engineering run (Run I) in November-December 2016, the detector was operated continuously between March and December, 2017 (Run II).

In order to assess the overall performance of the detector and the gas system while minimizing the effect of possible leaks as well as limiting the energy of potential sparks, the operational pressure in Run II was limited to 7.2 bar during the first part of the data taking run. The drift field was kept at 400 V cm^{-1} and the reduced field in the EL region at 1.7 kV cm^{-1} bar^{-1}, slightly below the expected nominal value of 2.2 kV cm^{-1} bar^{-1}. This translates into a gate voltage of 7.2 kV and a cathode voltage of 27 kV. Under those conditions, the chamber was extremely stable, with essentially no sparks recorded over the period.

During the second part of the run the pressure was raised to 9.1 bar and the voltages were correspondingly adjusted to keep approximately the same drift voltage and reduced field as during the first part of the run.

In this paper, we describe the calibration of the detector using a rubidium source (^{83}Rb) which provides a large sample of krypton (^{83m}Kr) decays, yielding a homogenous sample of 41.5 keV energy deposits. These point-like, evenly-distributed events permit to measure, correct for, and continuously monitor the drift-electron lifetime, as well as to measure and correct for the dependence of the measured energy on the transverse (x, y) coordinates. After correcting both effects, the energy resolution of the chamber for point-like energy deposits can be determined.

The paper is organized as follows: section 2 explains the principle of operation of a HPXe-EL and its intrinsic energy resolution; section 3 presents a brief description of the NEXT-White detector; section 4 describes how krypton calibrations are used to produce lifetime and energy maps; data processing and event selection are described in section 5; lifetime maps in section 6; energy maps in section 7; in section 8 the energy resolution measured with NEXT-White is presented; and finally, results are summarized in section 9.

2 Principle of operation and intrinsic resolution of a HPXe-EL TPC

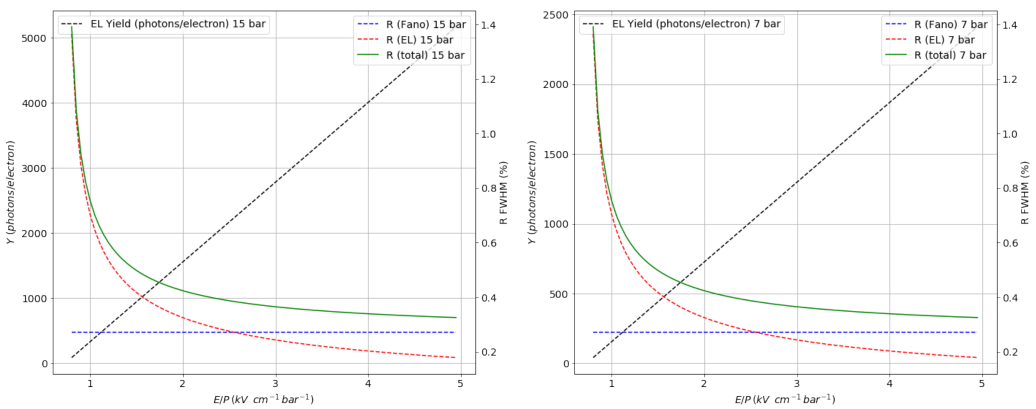

Figure 1: EL Yield and resolution terms characteristic of an HPXe-EL as a function of the reduced electric field for an EL gap of 6 mm and a value of $k \sim 0.006$ (see text for details). The left panel corresponds to a pressure of 15 bar. The right panel corresponds to a pressure of 7.2 bar.

As a charged particle propagates in the dense gas of a HPXe-ELTPC it loses energy by ionizing and exciting atoms of the medium. The excitation energy is manifested in the prompt emission of VUV (172 nm) scintillation light. The ionization electrons (ions) left behind by the particle are prevented from recombination and drifted towards the anode (cathode) by the action of a *drift field*. At the end of the field cage the drifting electrons enter the electroluminescent region (ELR), defined by a transparent mesh and a uniform layer of a titanium oxide compound (ITO) named gate and the anode, respectively. The thickness of the ELR as well as the voltage drop between gate and anode are chosen to provide a reasonably large amplification of the ionization signal without further ionizing the gas. An HPXe-EL is, therefore, an *optical TPC*, where both scintillation and ionization produce a light signal. In NEXT-White (and in NEXT-100), the light is detected by two independent sensor planes located behind the anode and the cathode. The energy of the event is measured by integrating the amplified EL signal (S_2) with a plane of photomultipliers (PMTs). This *energy plane* also records the primary scintillation light (S_1) which triggers the start-of-event (t_0). Electroluminescent light provides tracking as well, since it is detected a few mm away from production at the anode plane via a dense array of silicon photomultipliers (SiPMs), which constitute the *tracking plane*.

The reduced electroluminescent yield (*e.g.*, number of photons per ionization electron entering the EL region and unit of pressure), Y/P, of an HPXe-EL is experimentally found ([10]) to be:

$$Y/P = (136 \pm 1)(E/P) - (99 \pm 4)\ [\text{photons electron}^{-1}\ \text{cm}^{-1}\ \text{bar}^{-1}] \tag{2.1}$$

where E/P is the reduced field in the ELR.

One of the crucial features of an HPXe-EL TPC is its excellent intrinsic energy resolution, due to the small value of the Fano factor (F) [11] in gaseous xenon and the small fluctuations of the EL yield. Following [10] the resolution (FWHM) of an HPXe-EL can be written as:

$$R_E = 2.35\sqrt{\frac{F}{\bar{N}_e} + \frac{1}{\bar{N}_e}\left(\frac{J}{\bar{N}_{EL}}\right) + \frac{1.25}{\bar{N}_{ep}}} \tag{2.2}$$

where $\bar{N}_e$ is the number of primary ionization electrons created per event, J is the relative variance in the number of photons per ionization electron, $\bar{N}_{EL}$ is the number of photons produced per ionization electron and $\bar{N}_{ep}$ reflects the number of photoelectrons produced in the PMTs per event. The factor 1.25 takes into account both the conversion efficiency of VUV photons into photoelectrons and the fluctuations in the photoelectron multiplication gain. Thus, these terms represent the fluctuations in the number of primary electrons (a small number, given the low value of the Fano factor, F = 0.15, in gaseous xenon), the electroluminescence yield and in the PMTs response (which in turn depends on the light collection efficiency of the detector and the distribution of the PMT's single electron pulse height), respectively. In pure xenon $J/\bar{N}_{EL} \ll F$, therefore, equation 2.2 can be further simplified to [10]:

$$R_E = 2.35\sqrt{\frac{F}{\bar{N}_e} + \frac{1.25}{\bar{N}_{ep}}} \tag{2.3}$$

In equation 2.3 the Fano factor term gives the intrinsic energy resolution of xenon. For an energy of production of electron-ion pair of w = 21.9 eV and a value of the decay energy $Q_{\beta\beta}$ = 2458 keV, one finds:

$$N_E = \frac{Q_{\beta\beta}}{w} = 112\,237\,\text{electrons} \tag{2.4}$$

and thus the intrinsic xenon resolution term has a constant value:

$$R_{int} = 2.35\sqrt{\frac{F}{\bar{N}_e}} \sim 0.3\,\% \tag{2.5}$$

The second term, associated to the intrinsic detector resolution reads:

$$\bar{N}_{ep} = k\bar{N}_e\bar{N}_{EL} \tag{2.6}$$

where k is the fraction of EL photons produced per $\beta\beta0\nu$ decay that gives rise to the production of a photoelectron.

Figure1 shows the EL yield and the resolution terms for an HPXe-EL as a function of the reduced electric field for the following operational parameters: a) a pressure of 15 bar (7.2 bar) corresponding to the nominal pressure of NEXT-100 (pressure of initial operation of NEXT-White); b) an EL gap of 6 mm; and c) a value of $k \sim 0.006$ (corresponding to a light collection efficiency of 31%, which is the same for NEXT-100 and NEXT-White). Notice that, while the resolution keeps improving with increasing reduced field, the improvement above 2.2 kV cm^{-1} bar^{-1} (a value for which the resolution reaches 0.40 %) is very small, while the needed voltages at the gate become very large. For the initial operation of NEXT-White the reduced field is chosen to be 1.7 kV cm^{-1} bar^{-1}, in order to limit the gate voltage to moderate values (7.2 kV at a pressure of 7.2 bar and 8.5 kV at a pressure of 9.1 bar). Under these operating conditions, the intrinsic resolution of the chamber at $Q_{\beta\beta}$ (for point-like energy deposits) is 0.45 %.

3 Overview of the NEXT-White detector

Table 1: NEXT-White TPC parameters.

TPC parameter	Nominal	Run II (4734)	Run II (4841)
Pressure	15 bar	7.2 bar	9.1 bar
EL field (E/P)	2.2 kV cm^{-1} bar^{-1}	1.7 kV cm^{-1} bar^{-1}	1.7 kV cm^{-1} bar^{-1}
EL gap	6 mm	6 mm	6 mm
V_{gate}	16.2 kV	7.0 kV	8.5 kV
Length	664.5 mm	664.5 mm	664.5 mm
Diameter	454 mm	454 mm	454 mm
Fiducial mass	5 kg	2.3 kg	3 kg
Drift length	(530.3 ± 2.0) mm	(530.3 ± 2.0) mm	(530.3 ± 2.0) mm
Drift field	400 V cm^{-1}	400 V cm^{-1}	400 V cm^{-1}
$V_{cathode}$	41 kV	28 kV	30 kV

The NEXT-White detector has been thoroughly described elsewhere [12] and only a brief summary of its main features is offered here. It has three main subsystems, the TPC, the energy plane and the tracking plane. Table 1 shows the main parameters of the TPC. The energy plane is instrumented with 12 Hamamatsu R11410-10 PMTs located 130 mm behind the cathode, providing a coverage of 31%. The tracking plane is instrumented with 1792 SiPMs SensL series-C distributed in a square grid at a pitch of 10 mm. An ultra-pure 60 mm-thick copper shell (ICS) acts as a shield in the barrel region. The tracking plane and the energy plane are supported by 120 mm-thick pure copper plates.

The detector operates inside a pressure vessel fabricated with a radiopure titanium alloy (316Ti) surrounded by a lead shield. Since a long electron lifetime is a must, xenon circulates in a gas system where it is continuously purified. The whole setup sits on top of a tramex platform elevated over the ground in HALL-A of LSC.

4 Krypton calibrations

Figure 2 shows the decay scheme of a ^{83}Rb nucleus. The exotic rubidium isotope decays to ^{83m}Kr via electron capture with a lifetime of 82.2 days. The krypton then decays to the ground state via two consecutive electron conversions. The decay rate is dominated by the first conversion with a half-life of 1.83 h, while the second one has a very short half-life of 154.4 ns. The total released energy sums up to 41.5 keV and the ground state of ^{83}Kr is stable.

The rubidium source formed by a number of small (1 mm-diameter) zeolite balls stored in a dedicated section of the gas system. ^{83m}Kr nuclei produced after the electron capture of ^{83}Rb emanate from the zeolite and flow with the gas inside the chamber. The source has an intensity of 1 kBq. The rate of ^{83m}Kr decays is limited by the data acquisition to a comfortable value of about 10 Hz.

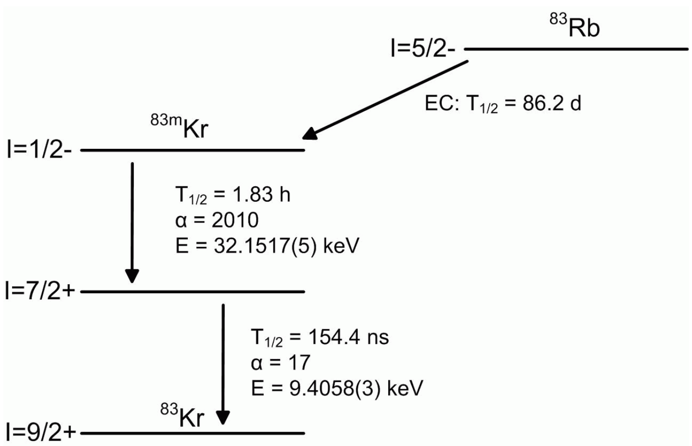

Figure 2: ^{83}Rb decay scheme.

A ^{83m}Kr decay results in a point-like energy deposition. The time elapsed before detection of S_1 and detection of S_2 is the drift time and its measurement, together with the known value of the drift velocity [13], determines the z-coordinate at which the ionization was produced in the active region. The (x, y) coordinate is obtained by a position reconstruction algorithm which uses the energies recorded by the SiPMs of the tracking plane. The combination of the PMT and SiPM sensor responses yields a full 3D event reconstruction.

To properly measure the energy of an event in NEXT-White it is necessary to correct for two instrumental effects: a) *the finite electron lifetime*, due to the attachment of ionization electrons drifting towards the cathode with residual impurities in the gas, and b) *the dependence of the light detected by the energy plane on the* (x, y) *position of the event*. Krypton calibrations provide a powerful tool to measure and correct both effects.

The effect of electron attachment is described using an exponential relation:

$$q(t) = q_0 \, e^{-t/\tau} \tag{4.1}$$

where q_0 is the charge produced by the ^{83m}Kr decay, t is the drift time, and τ is the lifetime. Ideally, attachment can be corrected by measuring a single number. However, in a high pressure detector the lifetime may depend on the position (x, y, z), due to the presence of non homogenous recirculation of the gas, or concentrations of impurities due to virtual leaks. As discussed in section 6, the dependence of τ with the longitudinal coordinate z in the NEXT-White detector can be neglected, while the dependence of τ with the transverse (x, y) coordinates must be taken into account. This is done using krypton calibrations to produce a *lifetime map* that records the lifetime as a function of (x, y).

Furthermore, ^{83m}Kr decays can be used to produce a map of energy corrections. This map is needed to properly equalize the energy of events occurring in different locations in the chamber as the light detected by the photomultipliers depends on the (x, y) coordinates of the event. Such dependence comes directly from the variation of the solid angle covered by the PMTs. The map cannot be computed analytically, since in addition to the direct light reaching the energy plane one has to include the light reflected by the light tube and other internal surfaces in the chamber.

This calibration method has already been studied and used by other experiments [14–16]. We report its first use in a gaseous detector.

5 Data processing and event selection

Trigger

The detector triggers on the Krypton S_2 signals. The uncorrected energy of the S_2 signals depends quite strongly on (x, y, z) given the sizable effect of both the spatial (x, y) corrections and the lifetime. However, as illustrated in figure 3, the range of the total energy measured by the photomultipliers is well defined between 5×10^3 pes and 15×10^3 pes. Events are triggered on the signal of two PMTs located at small radius. Each PMT records roughly 1/12 of the total light recorded. For this reason the trigger requires that the two central PMTs record a signal in the range 200 to 1500 photoelectrons (pes).

Waveform processing

The raw data are PMT and SiPM waveforms. The PMT waveforms are sampled each 25 ns, while the SiPM waveforms are sampled each 1 µs. The analysis proceeds according to the following steps.

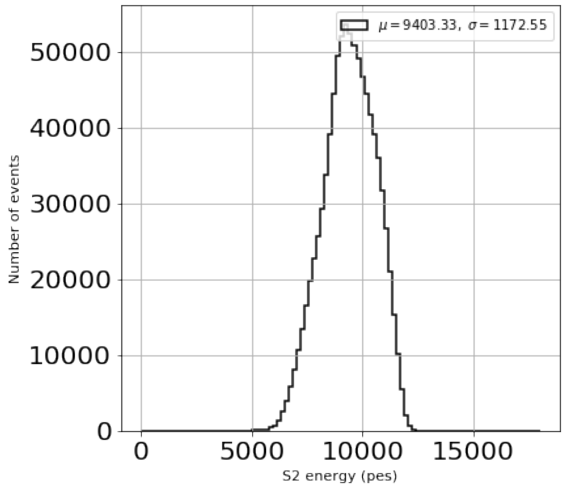

Figure 3: Left panel: Uncorrected S_2 energy (in photoelectrons) measured by the sum of the PMTs.

Deconvolution of the PMT raw waveforms

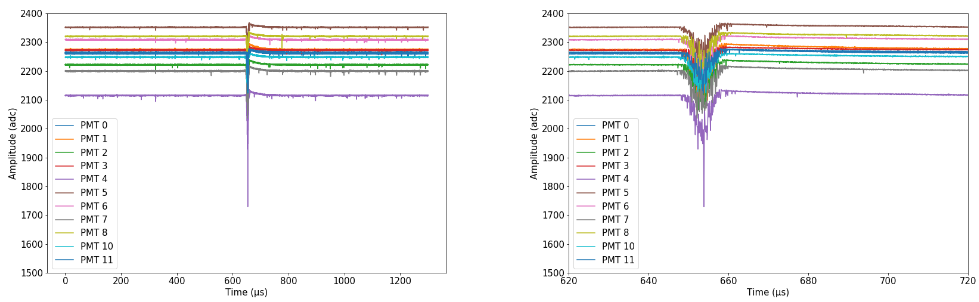

Figure 4: ^{83m}Kr raw waveforms for the individual PMTs, showing the negative swing introduced by the PMTs frond-end electronics. The left panel shows the RWF in the full DAQW, while the right panel shows a zoom on the S_2 signal on which the event was triggered.

As described in [12], the PMT waveforms show an opposite-sign swing due to the effect of the front-end electronics. The first step in the processing is to apply a deconvolution algorithm [12, 17], to the arbitrary-baseline, uncalibrated raw-waveforms (RWFs), to produce positive-only, zero-baseline, calibrated waveforms (CWFs). Figure 4 shows the RWFs corresponding to the PMTs of the energy plane, while Figure 5 shows the CWF waveform corresponding to the PMT sum. The event was triggered by the S_2 signal, which appears centered in the middle of the data acquisition window (DAQW). The S_1 signal appears at the beginning of the DAQW.

Search for S_1 signals

The first half of the CWF (drift time below 620 μs) is processed by a peak-finding algorithm tuned to find small signals. Each signal is characterized by its total energy (e_s), width (w_s), peak or height

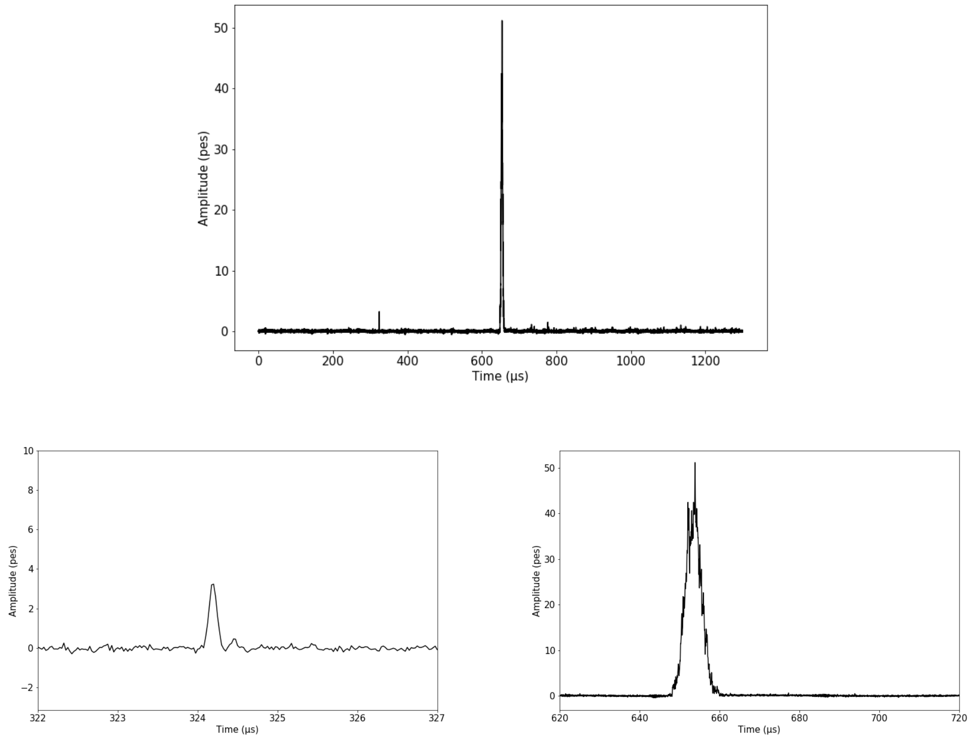

Figure 5: ^{83m}Kr corrected waveforms for the sum of the PMTs. The top panel shows the CWF in the full DAQW, while the bottom panels show zooms of the S_1 (left) and S_2 (right) waveforms.

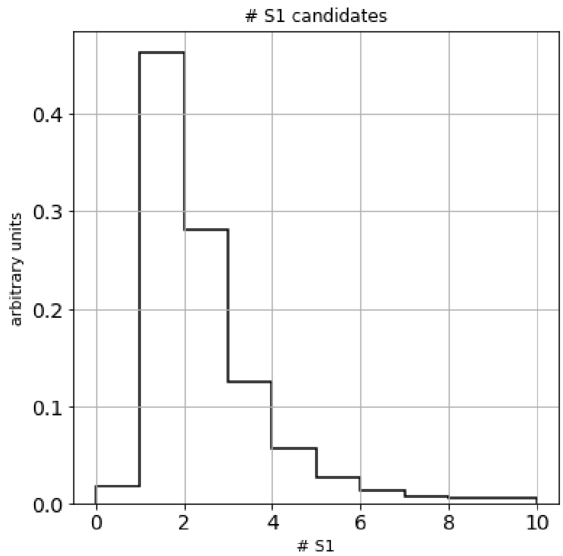

Figure 6: Number of S_1 candidates found by the peak-finding algorithm.

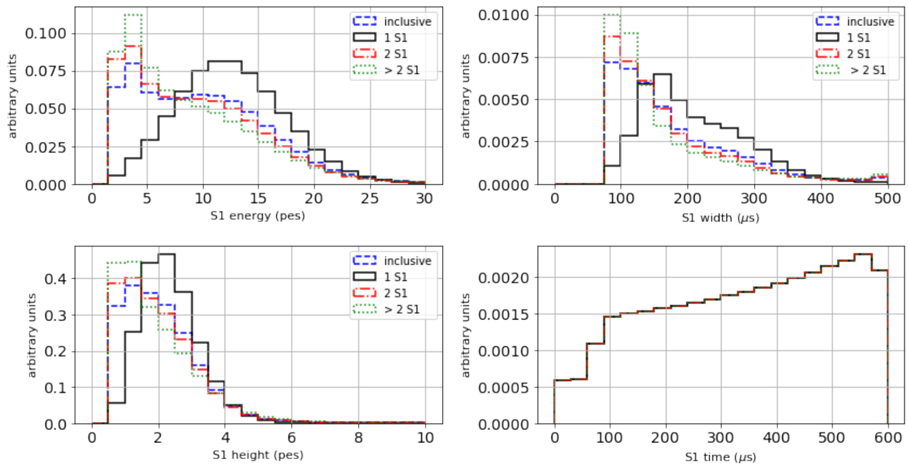

Figure 7: Distributions of S_1 candidates, from left to right and from top to bottom: e_s (energy), w_s (width), h_s (peak or height) and t_s (time). Blue (dashed) lines correspond to inclusive distributions (any number of S_1 candidates), black (solid) lines correspond to events with exactly one S_1. Red (dot-dashed) lines correspond to events with two S_1 candidates and green (dotted) lines to more than two S_1 candidates.

(h_s) and time (t_s), defined as the time corresponding to its height. The output of the algorithm is a list of S_1 candidates. The distribution of the number of candidates is shown in figure 6. A single S_1 is identified in about half of the events, while two S_1 candidates are identified in near 30% of the events and 3 or more candidates are identified in the remaining 20%. Figure 7 shows the corresponding e_s, w_s, h_s and t_s distributions. The one-S_1 sample is dominated by genuine S_1 signals, while the sample with two or more S_1 include fake signals associated with krypton events happening in the field-cage buffer, or small scintillation signals. Only events with exactly one S_1 candidate pass to the next stage of the selection.

The second half of the CWF (drift time greater than 620 µs) is then processed by the same peak finding algorithm, this time tuned to find larger signals. Most of the times a single S_2 candidate is found. Only events with exactly one S_1 and one S_2 are accepted for the analysis.

Position of the event

The z coordinate of the events is computed by multiplying the drift time (obtained as the difference between S_1 and S_2) by the drift velocity, v_d, which is also measured using the data themselves as described in [13]. The position and charge of each SiPM with signal above 10 pes (chosen to eliminate spurious hits due to SiPM dark noise) within the waveform range defined by the S_2 are used to calculate a local barycentre around the SiPM with maximum energy which estimates the (x, y) position of the event.

Figure 8 shows the distribution of events in the (x, y) plane, which is roughly uniform. The low-statistics pixels (dark blue color) correspond to inoperative or defective SiPMs. Figure 9 shows that the reconstruction algorithm is well behaved. The left panel shows the difference between reconstructed and true position, Δx, for Monte Carlo krypton events. The distribution is

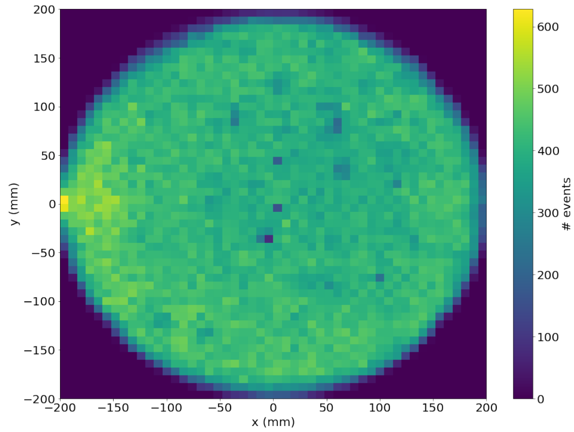

Figure 8: Distribution of events in the (x, y) plane.

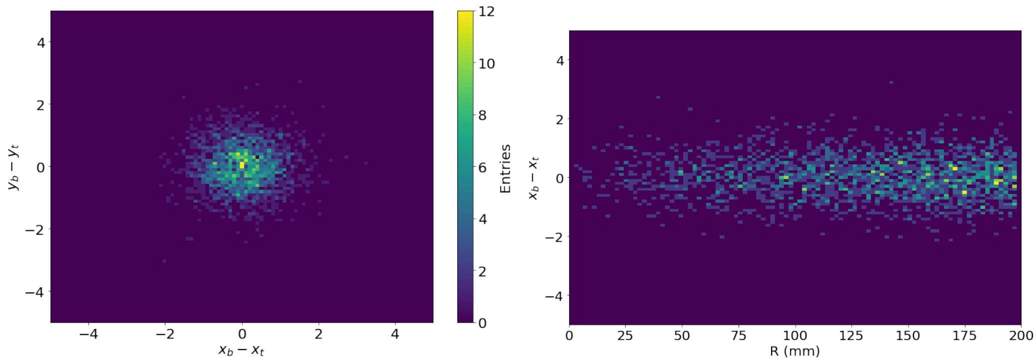

Figure 9: Left panel: difference between reconstructed and true position, Δx, for Monte Carlo krypton events; right panel: dependence of Δx with the radius, for x.

approximately gaussian in both the x and y coordinate, with an r.m.s of 0.7 mm. The right panel shows the dependence of Δx with the radius, for x (the behavior of y is identical), showing no bias with the radial position.

Datasets

The data used in this analysis were collected with NEXT-White in Fall 2017. Two runs are considered. Run 4734 started in October 10, 2017 and collected 2 687 860 events at a trigger rate of 10.5 Hz. The pressure was 7.2 bar, the cathode was held at 28 kV and the gate at 7.0 kV. Run 4841 started in November 16, 2017 and collected 2 993 867 events at a trigger rate of 8.2 Hz. The pressure was 9.1 bar, the cathode was held at 30 kV and the gate at 8.5 kV.

6 Lifetime maps

As stated in section 4, under certain conditions, (*e.g.* non homogenous recirculation of the gas, combined with concentrations of impurities due to virtual leaks) , the drift lifetime, τ, may depend on the (x, y, z) position.

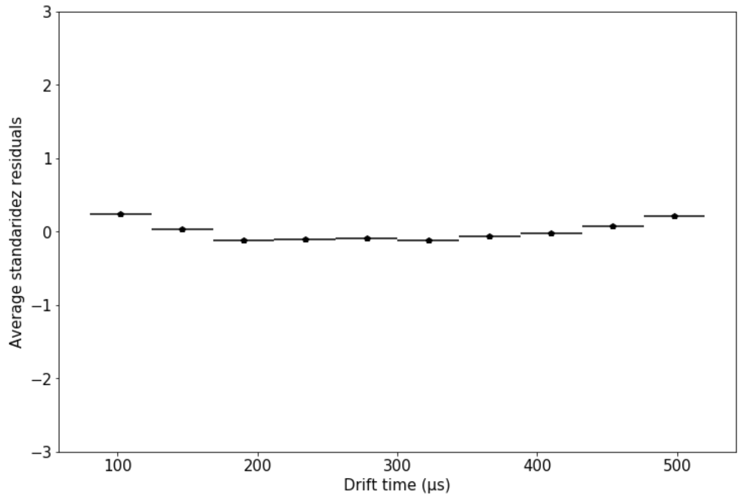

Figure 10: Average electron-lifetime (τ) residuals (R_z) as a function of z, showing that τ is practically constant along the longitudinal coordinate.

In NEXT-White the dependence of τ with z is found to be negligible. This is illustrated by figure 10, where the dependence of the average residuals, $R_z = \frac{\sum_{xy} r_z}{n_{xy}}$ is plotted as a function of z. To compute R_z the chamber is divided first in n_{xy} bins in the transverse coordinates (x, y). Each (x, y) bin is in turn divided in n_z bins. For each (x, y) bin, the residual $r_z = \frac{e_z - f(z)}{\sigma}$ is computed. This residual quantifies the difference (normalized to the measurement uncertainty, σ) between the energy measured in the corresponding z bin (e_z) and the expected value of the energy in the bin ($f(z)$) using a single τ, *e.g.*, $f(z) = e_0 e^{-t/(\tau v_d)}$, (where v_d is the drift velocity and e_0 the energy in the bin $z = 0$). As it can be seen, the dependence of R_z with z is very small, thus justifying the hypothesis than the τ does not depend on z. The data correspond to run 4734, but run 4845 shows the same behavior.

Instead, the lifetime is found to depend on (x, y) for run 4734. This effect is illustrated in figure 11 where lifetime fits for two regions are shown, one near the center, defined by x = [0, 50] mm, y = [0, 50] mm (left panel) and one in the upper edge, defined by x = [100, 150] mm, y = [100, 150] mm (right panel). Both fits yield a good χ^2/dof (1.2 for the first fit, 0.8 for the second), but considerably different lifetimes of (1788 ± 5) μs (near the center of the chamber) and (1941 ± 21) μs (near the top of the chamber).

This dependence of the lifetime can be corrected using large-statistics krypton runs to produce a *lifetime map*. The map is built by diviving the chamber in 60 × 60 bins, each bin being a 6.7 mm-size square and fitting for the lifetime in each bin. The number of bins is chosen to maximize granularity while still keeping enough data in each bin so that the statistical uncertainties of the fits are small.

The resulting maps are shown in figure 12 for run 4734. The optimal parameters found by fitting the data correspond to the prediction of the energy at $z = 0$ and its uncertainty, as well as the lifetime and its uncertainty. Thus, the map displayed in the top-left panel is an energy map, where the effect of the lifetime has been factored out, showing the dependence of the event energy on (x, y). The map is rather uniform in the central region, with the exception of a "crater" centered

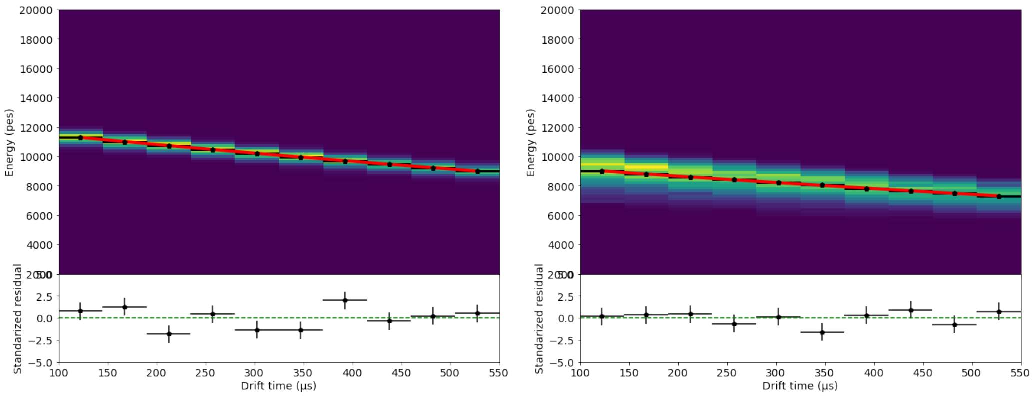

Figure 11: Exponential fits to the distribution of krypton energies as a function of the drift time in two different regions of the chamber. Left panel: in the region defined by x = [0, 50] mm, y = [0, 50] mm the lifetime is (1788 ± 5) µs. Right panel: in the region defined by x = [100, 150] mm, y = [100, 150] mm the lifetime is (1941 ± 21) µs

around [−50, 50] whose origin we attribute to a few SiPM boards with degraded reflectance, and fall abruptly at large radius, as the solid angle covered by the PMTs falls to zero. The lifetime map is shown in the bottom-left panel. A region of larger lifetime (close to 2 ms) appears at large positive y, near the top of the chamber (the average lifetime in the center of the chamber is around 300 µs smaller).

Figure 13 shows the same maps for run 4845, taken at 9.1 bar. The energy map still shows the crater in the same position, but the lifetime map is uniform, indicating that the possible virtual leaks present during run 4734 have vanished, the gas circulation is more homogeneous, or both.

The crucial point is that, while it is difficult to understand the complex physics that may lead to variable lifetime maps, krypton calibrations permit a correction for those effects.

7 Refining the energy map

The optimal parameters obtained by fitting for the lifetime in bins of (x, y) described in section 6 yield an energy map which describes the variations of the predicted energy (at $z = 0$) with the transverse position of the event. The map can be further refined dividing the (x, y) plane in smaller bins than those used for the lifetime fits and computing for each bin the sum of the PMT energies corrected by lifetime. The energy in each bin is then fitted to a Gaussian distribution that describes well the data. An example is shown in figure 14. The energy correction factor $f(x, y)$ is simply the inverse of the mean of the gaussian distribution in each (x, y) bin, normalized to a constant factor which can be chosen as the maximum energy bin.

Figure15 shows the energy map for run 4734 (the map for 4841 is essentially identical) compared with the energy map computed using Monte Carlo data. Notice that the behavior of the map at large radius, largely due to solid angle effects is well predicted by the Monte Carlo, but not the presence of the crater, which can only be corrected using calibration data. The uncertainties are very small (of the order of 0.3 %) introducing a small residual error in the energy correction,

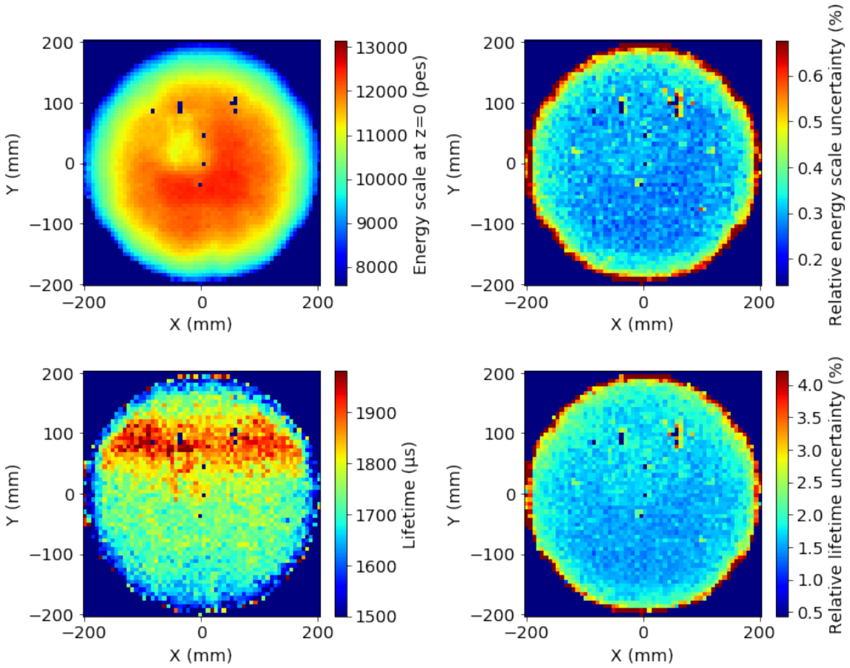

Figure 12: Maps obtained by fitting the lifetime as a function of (x, y) for run 4734. The predicted energies for $z = 0$ (left) and their uncertainties (right) are displayed in the top row, while the lifetimes (left panel) and their uncertainties (right panel) are shown in the bottom row. A clear dependence of the lifetime on (x, y) is observed. The uncertainty in the energy scale is of the order of 0.2 %, making a sub-dominant contribution to the energy resolution at 41.5 keV. On the other hand, the uncertainty in the lifetime value is of the order of the 1% and cannot be neglected for the interpretation of the final value of the energy resolution.

which for Run II is negligible compared with the residual error introduced by the lifetime correction, except at large radius where the angular coverage of the PMTs falls steeply.

8 Energy Resolution

To estimate the energy resolution for point like energy deposits in NEXT-White, the krypton data are divided in two samples. The *correction (C)* sample is used to compute the lifetime and geometry correction maps, which are then applied to the data in the *measurement (M)* sample. The corrected energy of the PMT sum is then fitted to a gaussian to estimate the energy resolution.

Even after corrections, the energy resolution is expected to depend on both the radial and the longitudinal coordinates. The dependence with the radius is related with the decreasing solid angle coverage, which means that PMTs record less light (thus larger fluctuations) for events happening at large R. The dependence with z is related with the loss of secondary electrons caused by attachment. A smaller number of electrons is associated with larger fluctuations and correction factors, which worsens the energy resolution as described in section 2.

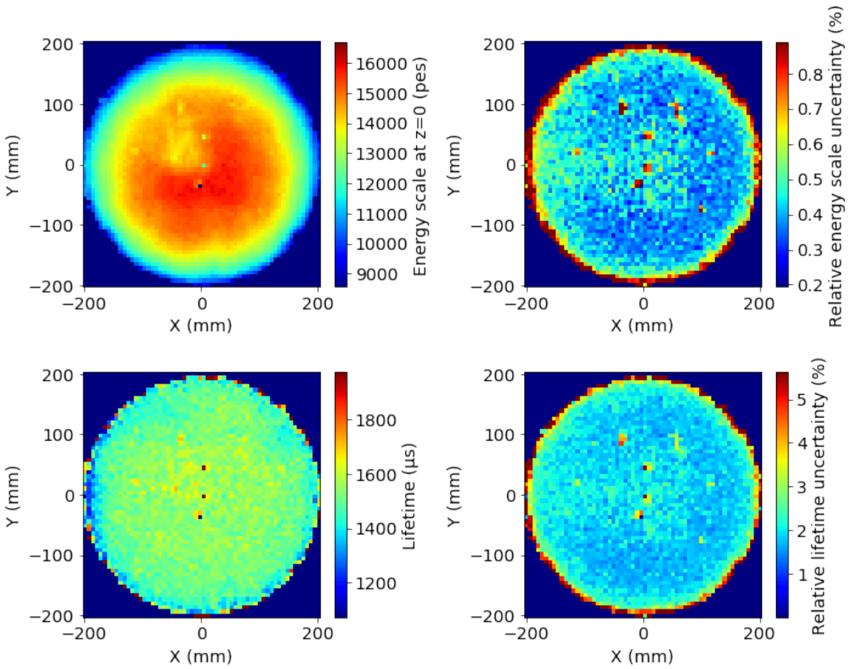

Figure 13: Maps obtained by fitting the lifetime as a function of (x, y) for run 4845. The energy map is statistically compatible with the one obtained with run 4734, while the lifetime map has become homogeneous.

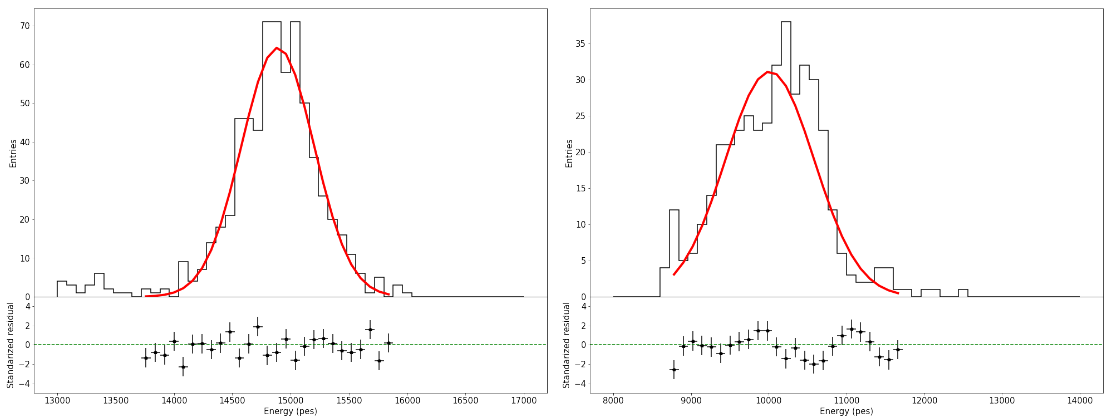

Figure 14: Fits to the lifetime-corrected energy in bins of (x, y) for run 4841. Left panel: x = [0, 10] mm, y = [0, 10] mm. The fit yields a mean value for the energy of (14 890 ± 13) pes, with $\chi^2 = 0.98$. Right panel: x = [140, 150] mm, y = [140, 150] mm. The fit yields a mean value for the energy of (10 011 ± 32) pes, with $\chi^2 = 1.04$.

The left panel of figure 16 shows the dependence of the energy resolution as a function of r, where it is possible to define 3 regions. A fiducial region up to R <150 mm, where the resolution is roughly flat, at around 4% FWHM. The resolution stays below 4.5 %, for R <175 mm, and degrades

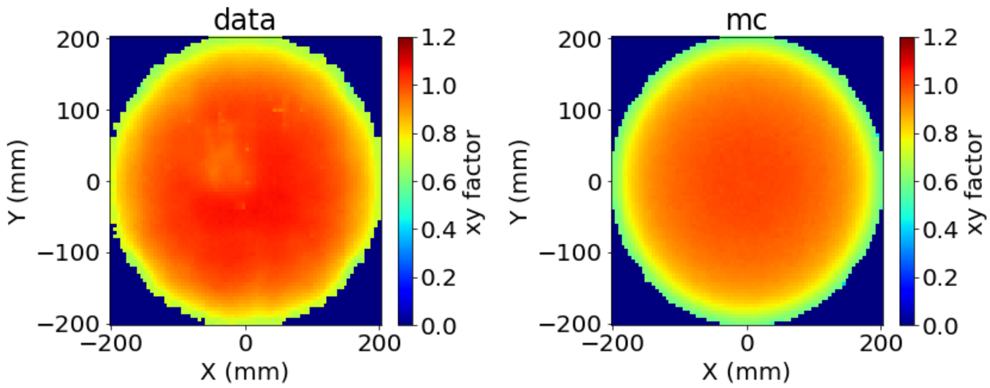

Figure 15: Energy map for run 4734 (left panel) and for MC data (right panel).

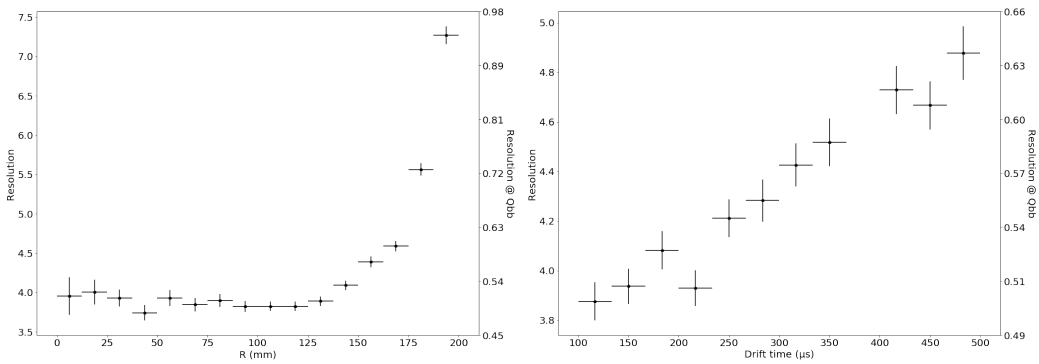

Figure 16: Left panel: dependence of the resolution with r. Right panel: dependence of the resolution with z.

rapidly for larger radial values. Since the total radial coverage of the chamber is 200 mm, this implies that an extended fiducial region of acceptable resolution extending up to 175 mm can be defined for physics analysis.

The PMT coverage improves as detector radial dimensions increases, since the region of low solid angle coverage corresponds essentially to the last PMT ring. Taking this into consideration, a considerably smaller reduction in fiducial volume is expected for NEXT-100 since only the last 10 mm to 15 mm of the total radius need be removed.

The right panel of figure 16 shows the dependence of the energy resolution as a function of z, which degrades with increased drift, although it stays always below 5% FWHM. The obvious implication is that long lifetimes are a must for TPC detectors striving to achieve excellent energy resolution.

Figure 17 illustrates the energy resolution measured with run 4734 (at a pressure of 7.2 bar). The data are fitted to a double-gaussian, to take into account tails due to residual background events (small energy deposits or ^{83m}Kr decays with wrong S_1 identification). The fit yields an energy resolution of (4.55 ± 0.01) % FWHM in the full NEXT-White volume (left panel). A naive $1/\sqrt{E}$

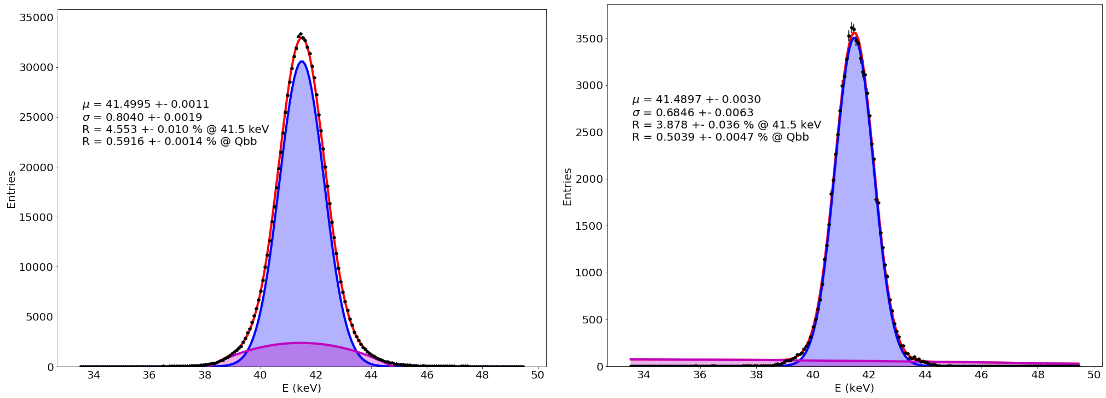

Figure 17: Corrected energy distribution for krypton events (left) in the full volume of the NEXT-White TPC, and in a restricted fiducial volume (right), for run 4734. See text for details.

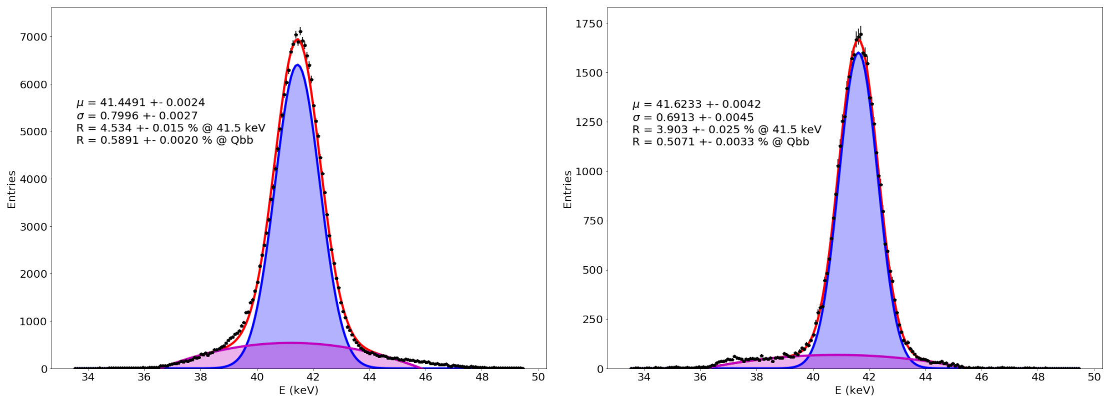

Figure 18: Corrected energy distribution for krypton events (left) in the full volume of the NEXT-White TPC, and in a restricted fiducial volume (right), for run 4841. See text for details.

extrapolation to $Q_{\beta\beta}$ yields $(0.592 \pm 0.001)\,\%$. The fit in the right panel corresponds to the data contained in a fiducial region defined by a radius smaller than 150 mm and z smaller than 150 mm. The radial cut ensures optimal geometrical coverage and the z cut minimizes the residual errors due to lifetime fluctuations, which increase with z. The fit yields $(3.88 \pm 0.04)\,\%$, extrapolating to $(0.504 \pm 0.005)\,\%$ at $Q_{\beta\beta}$. This value is reasonably close to the best resolution expected in NEXT-White (figure 1), confirming the excellent capabilities of the technology and the good working conditions of the chamber.

Figure 18 illustrates the energy resolution measured with run 4841 (at a pressure of 9.1 bar). The data are fitted to a gaussian plus a polynomial, to take into account tails due to residual background events (small energy deposits or ^{83m}Kr decays with wrong S_1 identification). The fit yields an energy resolution of $(4.53 \pm 0.02)\,\%$ FWHM in the full NEXT-White volume (left panel). A naive $1/\sqrt{E}$ extrapolation to $Q_{\beta\beta}$ yields $(0.589 \pm 0.002)\,\%$. The fit in the right panel corresponds to the data contained in the fiducial region defined above. The fit yields $(3.90 \pm 0.03)\,\%$, extrapolating to

(0.507 ± 0.003) % at $Q_{\beta\beta}$, similar to the values obtained for run 4734, and confirming that resolution for point-like energy deposits scales well with pressure.

The main systematic uncertainties in the energy resolution come from the uncertainties in the correction factors and the lifetime. We have estimated these uncertainties by measuring the variation in the energy resolution when those quantities are shifted $\pm 1\sigma$ around the optimal value. We find for both runs that the contribution is 0.04% at 41.5 keV. Taken this into account, we get a final estimate of the energy resolution in the full volume of (4.55 ± 0.04) % ((0.592 ± 0.005) % at $Q_{\beta\beta}$) for the 7.2 bar run and (4.53 ± 0.04) % ((0.589 ± 0.005) % at $Q_{\beta\beta}$) for the 9.1 bar run.

9 Summary

The NEXT-White detector has been calibrated using large samples of ^{83m}Kr decays taken near the end of the long calibration run (Run II) acquired in 2017. Two large data samples have been analyzed for this paper, run 4734 taken at a pressure of 7.2 bar, and run 4841 taken at 9.1 bar. The average lifetimes of the chamber were around 1.7 ms and 1.2 ms, respectively. In run 4734 a clear dependence of the lifetime with the transverse position (x, y) is observed, while run 4841 shows a constant lifetime in all the chamber. We observe that the energy map is in very good agreement with the Monte Carlo prediction, although it shows an unexpected valley of lower response near the center of the detector, presumably due to degraded reflectance in some SiPM boards. The effect of lifetime and solid angle is taken into account by correcting the data with lifetime and energy maps.

The measured energy resolution for point-like energy deposits in NEXT-White at 7.2 bar (run 4734) is (4.55 ± 0.04) % (which extrapolates $1/\sqrt{E}$ to (0.592 ± 0.005) %) in the full chamber and (3.88 ± 0.05) % ((0.504 ± 0.006) %) in a fiducial region ($r < 150$ mm, $z < 150$ mm) chosen to minimize the effect of lower solid angle coverage and large lifetime corrections. The energy resolution we obtain is remarkably close to the limit value for these conditions: 0.45 %. The energy resolution is essentially the same at 9.1 bar (run 4841). The results show the robustness of the technique to calibrate the NEXT-White detector as well as the excellent energy resolution characteristic of high pressure xenon chambers.

Acknowledgments

The NEXT Collaboration acknowledges support from the following agencies and institutions: the European Research Council (ERC) under the Advanced Grant 339787-NEXT; the Ministerio de Economía y Competitividad of Spain under grants FIS2014-53371-C04, the Severo Ochoa Program SEV-2014-0398 and the María de Maetzu Program MDM-2016-0692; the GVA of Spain under grants PROMETEO/2016/120 and SEJI/2017/011; the Portuguese FCT and FEDER through the program COMPETE, projects PTDC/FIS-NUC/2525/2014 and UID/FIS/04559/2013; the U.S. Department of Energy under contracts number DE-AC02-07CH11359 (Fermi National Accelerator Laboratory), DE-FG02-13ER42020 (Texas A&M) and de-sc0017721 (University of Texas at Arlington); and the University of Texas at Arlington. We acknowledge partial support from the European Union Horizon 2020 research and innovation programme under the Marie Sklodowska-Curie grant agreements No. 690575 and 674896. We also warmly acknowledge the the Laboratorio Nazionale di Gran Sasso (LNGS) and the Dark Side collaboration for their help with TPB coating of various parts of the

NEXT-White TPC. Finally, we are grateful to the Laboratorio Subterráneo de Canfranc for hosting and supporting the NEXT experiment.

References

[1] David Nygren. High-pressure xenon gas electroluminescent TPC for $0-\nu\beta\beta$-decay search. *Nucl.Instrum.Meth.*, A603:337–348, 2009.

[2] V. Álvarez et al. The NEXT-100 experiment for neutrinoless double beta decay searches (Conceptual Design Report). 2011.

[3] V. Álvarez et al. NEXT-100 Technical Design Report (TDR): Executive Summary. *JINST*, 7:T06001, 2012.

[4] J. J. Gomez-Cadenas et al. Present status and future perspectives of the NEXT experiment. *Adv. High Energy Phys.*, 2014:907067, 2014.

[5] J. Martín-Albo et al. Sensitivity of NEXT-100 to Neutrinoless Double Beta Decay. *JHEP*, 05:159, 2016.

[6] V. Álvarez et al. Initial results of NEXT-DEMO, a large-scale prototype of the NEXT-100 experiment. *JINST*, 8:P04002, 2013.

[7] V. Álvarez et al. Operation and first results of the NEXT-DEMO prototype using a silicon photomultiplier tracking array. *JINST*, 8:P09011, 2013.

[8] V. Álvarez et al. Near-Intrinsic Energy Resolution for 30 to 662 keV Gamma Rays in a High Pressure Xenon Electroluminescent TPC. *Nucl. Instrum. Meth.*, A708:101–114, 2012.

[9] P. Ferrario et al. First proof of topological signature in the high pressure xenon gas TPC with electroluminescence amplification for the NEXT experiment. *JHEP*, 01:104, 2016.

[10] C. A. B. Oliveira, M. Sorel, J. Martin-Albo, J. J. Gomez-Cadenas, A. L. Ferreira, et al. Energy Resolution studies for NEXT. *JINST*, 6:P05007, 2011.

[11] U. Fano. Ionization yield of radiations. ii. the fluctuations of the number of ions. *Phys. Rev.*, 72:26–29, Jul 1947.

[12] F. Monrabal et al. The NEXT-White detector. *JINST, in preparation*.

[13] A. Simón et al. Electron drift properties in high pressure gaseous xenon. *JINST, in preparation*.

[14] D. S. Akerib et al. $^{83\mathrm{m}}$Kr calibration of the 2013 LUX dark matter search. *Phys. Rev.*, D96(11):112009, 2017.

[15] L. W. Kastens, S. B. Cahn, A. Manzur, and D. N. McKinsey. Calibration of a liquid xenon detector with kr-83m. *Phys. Rev.*, C80:045809, 2009.

[16] W. H. Lippincott, S. B. Cahn, D. Gastler, L. W. Kastens, E. Kearns, et al. Calibration of liquid argon and neon detectors with $^{83}\mathrm{Kr}^{m}$. *Phys. Rev. C*, 81:045803, Apr 2010.

[17] V. Alvarez et al. The front-end electronics for the energy plane of the NEXT-White detector. *JINST, in preparation*.